

Article

A Selective Solar Absorber for Unconcentrated Solar Thermal Panels

Davide De Maio ^{1,2,†} , Carmine D'Alessandro ^{1,2,†} , Antonio Caldarelli ^{1,2} , Daniela De Luca ^{2,3} ,
Emiliano Di Gennaro ³ , Roberto Russo ^{2,*}  and Marilena Musto ¹ 

¹ Industrial Engineering Department, University of Napoli "Federico II", 80126 Napoli, Italy; davide.demaio@na.isasi.cnr.it (D.D.M.); carmine.dalessandro@na.isasi.cnr.it (C.D.); antonio.caldarelli@na.isasi.cnr.it (A.C.); marilena.musto@unina.it (M.M.)

² National Research Council of Italy, Napoli Unit, Institute of Applied Sciences and Intelligent Systems, 80131 Napoli, Italy; daniela.deluca@na.isasi.cnr.it

³ Physics Department, University of Napoli "Federico II", 80126 Napoli, Italy; emiliano.digennaro@unina.it

* Correspondence: roberto.russo@na.isasi.cnr.it

† These authors contributed equally to this work.

Abstract: A new Selective Solar Absorber, designed to improve the Sun-to-thermal conversion efficiency at mid temperatures in high vacuum flat thermal collectors, is presented. Efficiency has been evaluated by using analytical formulas and a numerical thermal model. Both results have been experimentally validated using a commercial absorber in a custom experimental set-up. The optimization procedure aimed at obtaining Selective Solar Absorber is presented and discussed in the case of a metal dielectric multilayer based on Cr_2O_3 and Ti. The importance of adopting a real spectral emissivity curve to estimate high thermal efficiency at high temperatures in a selective solar absorber is outlined. Optimized absorber multilayers can be 10% more efficient than the commercial alternative at 250 °C operating temperatures, reaching 400 °C stagnation temperature without Sun concentration confirming that high vacuum flat thermal collectors can give important contribution to the energy transition from fossil fuels to renewable energy for efficient heat production.

Keywords: thermal emittance; conversion efficiency; selective solar absorber; thermal energy; evacuated flat panel; solar energy



Citation: De Maio, D.; D'Alessandro, C.; Caldarelli, A.; De Luca, D.; Di Gennaro, E.; Russo, R.; Musto, M. A Selective Solar Absorber for Unconcentrated Solar Thermal Panels. *Energies* **2021**, *14*, 900. <https://doi.org/10.3390/en14040900>

Academic Editor: Gema San Vicente
Received: 8 January 2021
Accepted: 2 February 2021
Published: 9 February 2021

Publisher's Note: MDPI stays neutral with regard to jurisdictional claims in published maps and institutional affiliations.



Copyright: © 2021 by the authors. Licensee MDPI, Basel, Switzerland. This article is an open access article distributed under the terms and conditions of the Creative Commons Attribution (CC BY) license (<https://creativecommons.org/licenses/by/4.0/>).

1. Introduction

Solar energy plays a key role in the energy transition from fossil fuels to renewable energy [1]: several works showed that the adoption of energy-efficient and clean energy resources is crucial in reducing greenhouse gas emissions and pollution [2,3]. More than one fourth of the energy resources in the developed countries is nowadays used for heating and cooling [4,5], and industry represents a promising area of application [6]. Such a large fraction of energy can be provided by solar thermal collectors converting solar energy directly into heat with high efficiency. The core component of a solar thermal collector is the Selective Solar Absorber (SSA). An ideal SSA should perfectly absorb solar radiation (solar absorptance $\alpha = 1$), whereas its thermal emission should be minimal (thermal emittance $\varepsilon = 0$). However, the Kirchhoff's law of thermal radiation (Equation (1)) states that, for a given surface, in thermodynamic equilibrium, absorptivity and emissivity must be equal [7]

$$\alpha_{\lambda}(\lambda) = \varepsilon_{\lambda}(\lambda). \quad (1)$$

Moreover, in samples with zero transmissivity the energy conservation implies that the reflectivity is the complement of absorptivity, as in the following Equation (2)

$$\alpha_{\lambda}(\lambda) = \varepsilon_{\lambda}(\lambda) = 1 - \rho_{\lambda}(\lambda). \quad (2)$$

The Kirchhoff's law has been demonstrated to be valid on several surfaces and solar absorbers, including layered black metals [8,9]. Solar absorptance and temperature dependent thermal emittance (also referred as spectrally averaged absorptivity and spectrally averaged emissivity) are then calculated from the spectral emissivity curves as in the following Equations (3) and (4):

$$\alpha_S = \frac{\int_{0.3\mu\text{m}}^{2.5\mu\text{m}} \alpha(\lambda) \cdot S_{Sun}(\lambda) d\lambda}{\int_{0.3\mu\text{m}}^{2.5\mu\text{m}} S_{Sun}(\lambda) d\lambda}, \quad (3)$$

$$\varepsilon(T) = \frac{\int \varepsilon(\lambda) \cdot E_{bb}(\lambda, T) d\lambda}{\int E_{bb}(\lambda, T) d\lambda}, \quad (4)$$

with S_{Sun} and E_{bb} being the solar spectral irradiance and the blackbody radiation, respectively. The integral is calculated in the wavelength regions where $S_{Sun}(\lambda)$ and $E_{bb}(\lambda, T)$ are different from zero.

As consequence, the ideal SSA spectral emissivity is assumed to be a step function which flips from 1 to 0 [10] and the wavelength at which the transition happens is commonly named cut-off wavelength ($\lambda_{cut-off}$) [7,11]. The formal definition of $\lambda_{cut-off}$ leads to energetic considerations: it is the wavelength that maximizes the absorber thermal performance and it depends on the working temperature and on the solar incoming power (i.e., solar concentration ratio) [12]. It was generally verified that $\lambda_{cut-off}$ is the wavelength at which the blackbody emission curve crosses the solar radiation spectrum [11,13].

At low temperature, blackbody emission and solar spectrum barely overlap, and the optimization of the SSA limits the maximization of the solar absorption, since the demanded emissivity transition (from high absorptance in solar range and low thermal emittance in black body emission spectrum) is easily reached in a wide wavelengths range. When the operating temperature increases over 200 °C, the blackbody emission starts to overlap the solar spectrum and the sharpness of the transition assumes a greater importance.

The SSA idea was introduced at the end of 1950, and thenceforward several works have been devoted to SSA optimization [10,14]. To realize an SSA with an emissivity curve close to the ideal one, different designs have been analyzed by several authors in the past years [15,16]: nanomultilayer [17], ceramic and metal structures (known as cermet) [13], multilayers [18–20], photonic designs [21], structured graphene metamaterial [22], multilayered cermets [12]. However, a very sharp transition was never obtained and recently Yang et al. [23] studied the effect of non-ideal SSA properties on the overall performances in a Concentrated Solar Power (CSP) system: their simulated SSA has a finite constant slope in the cut-off transition (instead of the ideal step function) and a not ideal SSA emissivity. Dealing with a real SSA, the relative importance of solar absorptance and thermal emittance to calculate the absorber efficiency has to be taken into account. Cao [13] introduced a Weighting Factor, (w), that indicates the relative weight of α and $\varepsilon(T)$ in the efficiency of a solar absorber. In Figure 1a w is reported as a function of the absorber temperature and solar concentration.

All the previous selective absorbers, in literature as in commerce, were optimized for concentrated collectors or flat plate collectors without vacuum insulation: in this conditions $w < 1$ and hence α weights more than $\varepsilon(T)$. The only exception is [24], which obtained a stagnation temperature of about 230 °C under vacuum that could be increased to about 300 °C with further optimization.

The importance of vacuum insulation in a solar thermal panel has already been highlighted [25]; however, only recently TVP Solar [26] presented a new High Vacuum insulated Flat plate solar thermal Panel (HVFP) [27]. High vacuum insulation reduces the internal gas convective and conductive losses to a negligible level, keeping high conversion efficiency at high working temperature. In this case the thermal radiation is the main loss mechanism and the radiative properties of SSA are an aspect of primary importance. It is worth noting that thermal emittance gains weight over the absorptance as the working

temperature increases (green arrow in Figure 1a) and that HVFPs represent the only commercial product with $w > 1$. Several absorbers are commercially available, such as Mirotherm and Sunselect from Alanod [28], and several types of Tinox from Almeco [29]. They are based on cermet structures with lower and higher metal content to enhance the absorptance [13]. When tested in unconcentrated solar panels under high vacuum they do not differ in a significant way from each other with a stagnation temperature of about 310 °C [30]. Currently HVFPs include the absorber Mirotherm® from Alanod, a commercial SSA optimized for low working temperatures (up to about 150 °C). It results in excellent performance up to 180 °C, but at higher temperatures the low selectivity of the absorber increases the thermal radiation losses, affecting the panel efficiency and limiting the stagnation temperature at about 320 °C with an illumination of 1000 W/m². The increased panel efficiency due to high vacuum has been studied also from other researchers [31] and the superior performance up to 250 °C have been predicted [32], if an optimized SSA was mounted in HVFP. However, the authors did not give any indication on how to produce such optimized SSA.

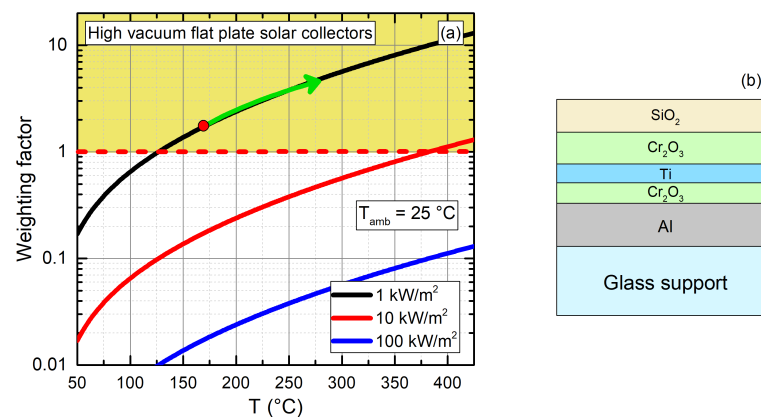


Figure 1. (a) Weighting factor versus absorber temperature T (°C) for different solar concentration ratios. The red dot indicates the operating temperature (160 °C) of High Vacuum insulated Flat plate solar thermal Panel (HVFP) equipped with commercial absorber and the green arrow the increasing importance of thermal emittance with working temperature (adapted from [13]). (b) Schematic structure of the multilayer under study. From bottom to top: glass substrate, aluminum film (250 nm) and its natural oxide, Chromium oxide Cr₂O₃, Titanium Ti, Chromium oxide Cr₂O₃ and silicon dioxide SiO₂.

In this work, a new absorber coating optimized to work at mid temperature in a high-vacuum system without concentration was developed. Multilayer absorbers were chosen, since they allow us to control thermal emission while guaranteeing high solar absorption and excellent thermal stability [33]. The new SSA is based on Cr₂O₃/Ti/Cr₂O₃ trilayer. The Cr₂O₃/Cr structure has been already deeply studied in form of cermet and it also used in some commercial absorber such as Mirotherm. The multilayer Cr₂O₃/Cr/Cr₂O₃ deposited by e-beam has also been studied: it presents quite good optical properties [18] and good thermal stability [34]. The chromium metallic layer has been replaced with titanium with the aim to improve the limited solar absorptance reported in previous works [18,34].

A single SiO₂ layer is used as antireflective coating to improve absorptance; a sketch of absorber structure is reported in Figure 1b. The simulated spectral emissivity curves are used to evaluate the temperature dependent thermal emittance which in turn allows us to evaluate the radiative losses and the SSA efficiency. The efficiency of the new absorber is discussed in comparison with the efficiency of commercially available absorber currently used in HVFPs. The optimized absorber has been deposited by e-beam on aluminum on glass substrate and the results are reported.

2. Materials and Methods

Multilayer SSAs consist of stacks of alternating dielectric layers (high absorptance in the visible range, transparent in the Infrared region) and metal absorption layers (thin enough to allow for partial transparency). Absorption is guaranteed by multiple reflections at interfaces, while thermal emittance is mainly due to the low-emissive metal substrate (IR reflector) [19,33,35]. In this study a tri-layered structure has been investigated. A Titanium absorbing layer is sandwiched between two Chromium Oxide (Cr_2O_3) dielectric layers on an aluminum substrate acting as IR reflector. Al_2O_3 natural passivation layer of the Al substrate has been included in the numerical simulations model. The multilayer structure is completed by an antireflective coating (ARC) based on SiO_2 to further enhance solar absorption.

The complex refractive index of the materials used to simulate the solar selective absorber have been experimentally determined. The materials were deposited by e-beam evaporation on an aluminum film on glass substrate and their complex refractive index were experimentally estimated by ellipsometry measurement [36].

2.1. Samples Preparation

The materials composing the multilayer solar absorber coatings were deposited on smooth glass substrates (roughness 1 nm) using e-beam evaporation physical deposition technique. The glass slides (TED Pella inc. #260230 made from optical grade soda lime glass) were cut in pieces of 25 mm \times 50 mm and cleaned using soapy water and ultrasonic washing in acetone and isopropanol baths. Substrates temperature was monitored during the deposition process and it never exceeded 80 °C. The e-beam system used is equipped with a rotating planetary that guarantees the samples thickness uniformity and the deposition of several substrates in the same conditions (see Figure 2).



Figure 2. E-beam deposition system: glass substrates mounted on the rotating planetary. The thickness monitor sensor is also visible.

The evaporating materials are Al, (Cr_2O_3) and Ti pellets with a purity of 99.999%. Prior to depositions, the vacuum chamber was pumped down to a base pressure of 10^{-5} Pa and the materials were slowly outgassed to remove unwanted trapped gases (impurities).

The deposition was controlled by a thickness monitor (Inficon model XTC/3) based on an exposed oscillating quartz crystal whose frequency decreases as material accumulates. The tooling factor of the thickness monitor was calibrated depositing a thicker layer (about 500 nm) that was measured using a profilometer (KLA Tencor P-15). The step to be measured was obtained by lift-off procedure in acetone, using standard photolithographic technique.

Evaporation rates were set on 0.2 nm/s for Al and Ti layers and on 0.1 nm/s for Cr_2O_3 layer. The thickness monitor controls the e-beam current, to keep the evaporation rate constant, as well as a shutter that stops the deposition once the desired thickness has been

deposited. A careful calibration allowed us to obtain a thickness control in the order of 1 nm. To facilitate optical studies all coatings have been deposited on aluminum coated glass substrates that have been exposed to air in order to obtain a reproducible Al_2O_3 natural passivation layer similar to that of the commercial aluminum rolls. The final SiO_2 anti-reflective layer was deposited by RF magnetron sputtering from a four inches high purity (99.995%) SiO_2 target. The deposition was performed at 200 W in a pure argon atmosphere (Ar pressure 2.5×10^{-1} Pa) and deposition rate was 0.11 nm/s, determined using the same procedure described before.

2.2. Samples Characterization

Aluminum film thickness has been chosen to be optical opaque and fixed to 250 nm for all produced samples. The Cr_2O_3 layer thicknesses have been varied from 5 nm up to 200 nm to study the possible influence of layer thickness on the optical properties. The film thickness was measured using a profilometer (KLA Tencor P-15) with scan repeatability 0.8 nm or 0.1% of step height, whichever is greater, and the reproducibility is 1.5 nm or 0.25% of step height, whichever is greater. The measured heights were then confirmed by ellipsometric analysis. The refractive index of the coatings were investigated using a phase modulated spectroscopic ellipsometer (UVISSEL by Jobin Yvon Horiba). The ellipsometer is equipped with a xenon lamp and two detectors: it can analyze the optical response in the wavelength range from 190 nm to 2100 nm. In the optical model the dispersion of the Cr_2O_3 the Forouhi-Bloomer formulation [37] was verified to reproduce our data very well, while Titanium was well described by a classical Drude dispersion model. For Aluminum, Al_2O_3 and SiO_2 layers literature data have been used [38–40] since from optical analysis they proved to fit well experimental data. Figure 3a,b reports the refractive index obtained by the characterization procedure and used in the numerical simulation of the multilayer solar absorber coating. The reported refractive index was able to fit Cr_2O_3 layer from 15 nm up to 200 nm and was obtained fitting 6 different samples. The use of glass substrates allows us to obtain very smooth surfaces and, as consequence, the optical response can be fitted without including any surface roughness. The refractive index data outside the explored wavelength range were extrapolated using the theoretical model [36].

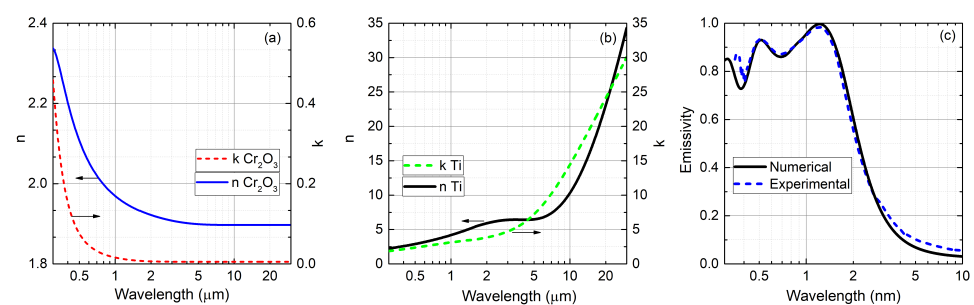


Figure 3. (a,b) Complex refractive index for Cr_2O_3 and Ti respectively: real part n on the left axis, imaginary part k on the right axis. (c) Emissivity curve of $\text{Cr}_2\text{O}_3/\text{Ti}/\text{Cr}_2\text{O}_3$ multilayer: experimentally measured absorptance (blue dotted line) and numerical simulation (black line).

Before proceeding with the multilayer optimization, it has been verified that the measured refractive indices and the numerical simulation program provide the correct multilayer optical response. Numerical simulations have been performed using IMD software [41], which allows us to estimate the optical response of a multi-layer structure. A multilayer with the following layer thicknesses: 70/10/70 nm has been first simulated and then deposited on aluminum on glass substrate by e-beam evaporation (the ARC layer was not deposited in this case). In Figure 3c are reported the numerical simulation and the experimental measurements showing the good agreement. The experimental optical response of the produced multilayer has been measured from 300 nm to 10 μm . To cover the whole spectral range we used an Optical Spectrum Analyzer (OSA) (300 nm up to

1700 nm) and a Fourier-Transform InfraRed (FTIR) spectroscopy (from 1200 nm up to 10 μm). The almost perfect agreement in the overlapping region confirms the measurement quality as well as the simulation and deposition accuracy.

2.3. Optimization Procedure

A genetic algorithm is used to adjust layer thicknesses, including the ARC layer, in order to fit a target curve. The genetic algorithm creates a starting population of individuals (in our case multilayers with different layer thicknesses) and a Figure of Merit (FOM) is determined; only individuals with best FOM will be retained. FOM function is defined as follows in Equation (5):

$$FOM = \frac{\sum_{i=1}^{N_{mo}} w[i] \cdot |Y[i] - Y_{mo}[i]|^n}{\sum_{i=1}^{N_{mo}} w[i]} \quad (5)$$

where $w[i]$ is the weighting factor for the i th point, $Y[i]$ is the value of the function being optimized for the i th point, $Y_{mo}[i]$ is the value of the target function for the i th point. $\Delta(FOM)/FOM < \zeta$ (with ζ the convergence tolerance value) determines the convergence of the algorithm. $\Delta(FOM) = \langle FOM \rangle - FOM$ and the quantity $\langle FOM \rangle$ corresponds to the average of FOM over the previous X generations of individuals. The exponent n has been set equal to 2.

The spectral emissivity curve of an ideal selective solar absorber with a temperature dependent $\lambda_{cut-off}$ defined as in [13] was used as a target function (Y_{mo}). Y functions, representing individuals spectral emissivity curves, are calculated by optical simulations once multi-layer materials thicknesses and the ARC layer thickness are fixed.

2.4. The Mini-Test-Box Set-Up

The Mini-Test-Box (MTB) is a custom experimental apparatus used to measure the absorptance and thermal emittance of SSA in operating conditions. It consists of a stainless steel high-vacuum chamber, closed by an extra-clear float glass, which can host a flat absorber suspended by four springs of negligible thermal conductivity. A detailed description of the measurement can be found in [42,43]. The behaviour of an absorber mounted in the MTB has been numerically simulated using Comsol Multiphysics [44]. In present work the experimental data were obtained illuminating the absorber with different light power using a calibrated LED illumination system described in [45] and recording the absorber stagnation temperature. In such configuration the power losses are equal to absorbed power $\varepsilon(T_{AS}) \cdot \sigma_{SB}(T_{AS}^4 - T_{amb}^4) + \varepsilon_{Sub} \cdot \sigma_{SB}(T_{AS}^4 - T_{amb}^4) = \tau_{Glass} \alpha_{LED} P_{LED}(T_{AS})$, where α_{LED} is the absorptance α evaluated as in Equation (3), where the solar spectrum is replaced by the spectrum of the LED lump used to illuminate the absorber [41], $P_{LED}(T_{AS})$ is the light power provided by the calibrated LED system and T_{AS} is the absorber stagnation temperature at the given LED power. As consequence, at $T = T_{AS}$ the efficiency can be calculated, as reported below in Equation (6):

$$\eta(T) = \tau_{Glass} \cdot \alpha_S - \frac{\tau_{glass} \cdot \alpha_{LED} \cdot P_{LED}(T_{AS})}{H_{abs}} \quad (6)$$

where H_{abs} is Sun irradiated power set to 1000 Wm^{-2} , $\tau_{glass} = 0.91$, $\alpha_S = 0.95$ in the case of Mirotherm.

3. Results and Discussion

The optimization procedure described in Section 2.3 has been repeated for four working temperature from 200 $^{\circ}\text{C}$ up to 350 $^{\circ}\text{C}$, corresponding to different optimal $\lambda_{cut-off}$. Table 1 sums up the values of $\lambda_{cut-off}$, layer thicknesses, solar absorptance α_S , and thermal emittance $\varepsilon(T)$ for each selective coating, as resulting from the optimization procedure. In the Table 1 are also reported Mirotherm solar absorptance and thermal emittance.

Reported values have been obtained measuring the emissivity curve as described in Section 2.2 and they are in agreement with values declared from the producer [28].

Table 1. Optimization temperature, $\lambda_{cut-off}$ for desired operating temperature, layer thickness obtained from the optimization process, solar absorptance α_S and thermal emittance $\varepsilon(T)$ at 200 °C, 250 °C, 300 °C and 350 °C calculated from Equations (3) and 4, for 5 multilayer absorbers. Sample E was designed to have a $\lambda_{cut-off} = 1.50 \mu\text{m}$. In the last column the absorptance and emittance values of Mirotherm are reported [28].

Sample	A	B	C	D	E	Mirotherm
Optimization Temperature (°C)	200	250	300	350	-	-
$\lambda_{cut-off}$ [13] (μm)	2.47	2.37	2.19	1.79	1.50	≈ 2.5
Top dielectric layer thickness (nm)	110	98	81	59	46	-
Metal layer thickness (nm)	16	16	15	13	12	-
Bottom dielectric layer thickness (nm)	42	38	32	25	20	-
SiO ₂ Anti-Reflective Coating (nm)	70	67	63	60	52	-
Solar absorptance α_S	0.91	0.91	0.91	0.89	0.86	0.95
Thermal Emittance ε (200 °C)	0.056	0.050	0.041	0.031	0.026	0.058
Thermal Emittance ε (250 °C)	0.067	0.060	0.048	0.035	0.029	0.067
Thermal Emittance ε (300 °C)	0.080	0.071	0.057	0.041	0.034	0.076
Thermal Emittance ε (350 °C)	0.094	0.083	0.066	0.047	0.038	0.087

Figure 4a shows the spectral emissivity curve of the four optimized multi-layer absorbers and the emissivity curve resulting from the optimization process obtained for $\lambda_{cut-off} = 1.50 \mu\text{m}$. The results are compared with the Mirotherm commercial absorber (blue line with square markers in Figure 4) and they show that the SSA $\lambda_{cut-off}$ can be adjusted by varying the layer thicknesses, preserving a high solar absorption and a low thermal emission.

In Figure 4b, the temperature dependent thermal emittance of multi-layers, calculated according to Equation (4), is compared with the commercial coating currently used in high-vacuum solar collectors (blue line with dots). Multi-layers with lower $\lambda_{cut-off}$ can reduce the thermal emittance and its temperature dependence, resulting in a more than 50% emittance reduction at all temperature values.

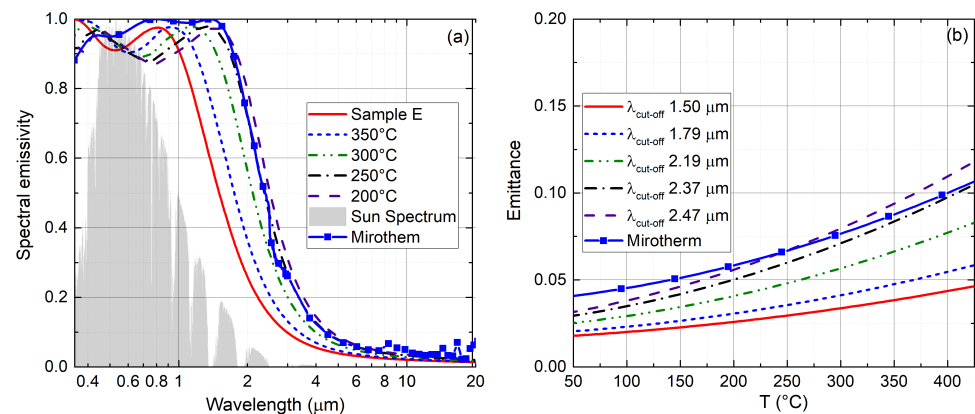


Figure 4. (a) Spectral emissivity of multilayer selective absorbers optimized for different temperature and consequent $\lambda_{cut-off}$ compared with the emissivity curve of the commercial coating (blue line with square markers). (b) Temperature dependent emittance for different $\lambda_{cut-off}$ calculated using Equation (4).

The SSA efficiency can be written as following:

$$\eta_{coat} = \frac{q_h}{H_{abs}} = \alpha_S - \frac{\varepsilon(T) \cdot \sigma_{SB}(T^4 - T_{amb}^4)}{H_{abs}} \quad (7)$$

where η_{coat} is the coating efficiency, α_S the solar absorptance, $\varepsilon(T)$ the temperature dependent thermal emittance, q_h the heat flux to the thermal system (Wm^{-2}), T the absorber temperature (K), T_{amb} the environmental temperature (K), and σ_{SB} the Stefan-Boltzmann constant ($\text{Wm}^{-2}\text{K}^{-4}$).

The SSA efficiency for the simulated multilayers and the commercial absorber, calculated from Equation (7), is plotted in Figure 5. The graph shows how temperature dependent thermal emittance shapes the selective absorber performance curves. Mirotherm® commercial absorber is optimized for standard flat-plate solar collectors: it shows the highest efficiency for lower values of operating temperature because of its higher solar absorption coefficient and a relatively low thermal emittance (see Figure 4b). Multilayers A and B are good options for mid temperature applications: although these two coatings have a lower solar absorptance α_S with respect to the commercial absorber, the improvement in thermal emittance (Figure 4b, Table 1) results comparable performances for high working temperatures. Multilayer C and D offer the highest stagnation temperatures thanks to the lowest thermal emittance, but a slightly lower efficiency in low to mid temperatures range. This is due to the low cut-off that reduces the power achievable from the Sun spectrum, resulting in a lower absorptance. However, starting from 200 °C, they present a coating efficiency higher than the other absorbers, including the Mirotherm®.

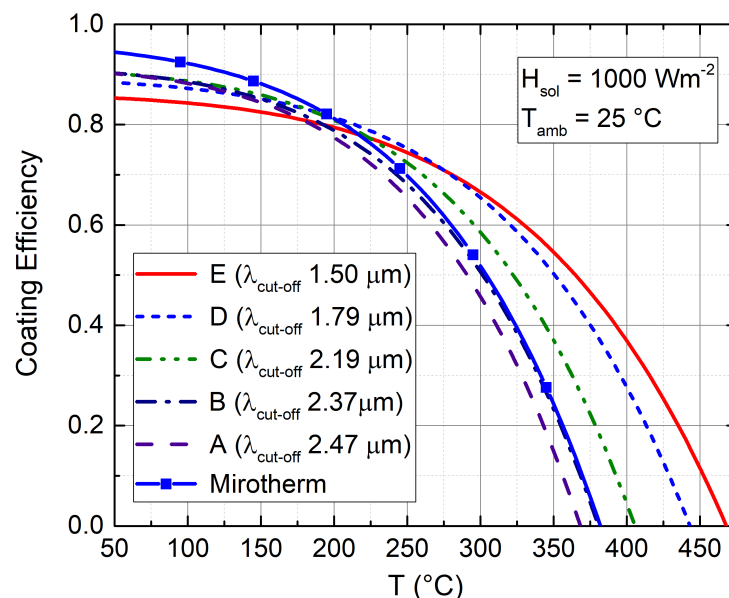


Figure 5. Absorber efficiency versus operating temperature for five multilayer absorbers with different $\lambda_{cut-off}$ optimized for different temperatures, and Mirotherm® commercial absorber (blue line with square markers).

In Figure 5 is also reported the efficiency of sample E, whose spectral emissivity was designed to have a $\lambda_{cut-off} = 1.5 \mu\text{m}$. Its cut-off is outside the typically explored wavelength interval, since it corresponds to a region of zero intensity in the Sun spectrum, one of the so-called *hidden regions* [13]. Despite the relative low absorptance of sample E (0.86 respect to 0.95 for Mirotherm), starting from 220 °C, its coating efficiency is higher than Mirotherm thanks to its lower thermal emittance (0.029 respect to 0.067 of Mirotherm).

A further reduction in $\lambda_{cut-off}$ below 1.5 μm can result in a further increase in the stagnation temperature, but drastically reduces the efficiency at lower temperatures (the curves are not reported here). This is due to the specific features of the solar irradiance spectrum, which rises very fast when wavelength reduces below 1.4 μm .

Equation (7) allows us to evaluate the coating efficiency without taking into account boundary conditions (such as the glass optical losses, conductive losses and substrate radiative losses due to the heat exchange between the back side of the absorber and the

collector vessel). In case of negligible conductive and convective losses (as in the case of an absorber suspended in a high vacuum envelope), Equation (7) can be modified in order to evaluate the overall absorber efficiency, η_{all} of a flat absorber as following:

$$\eta_{all} = \tau_{Glass} \cdot \alpha_S - \frac{\varepsilon(T) \cdot \sigma_{SB}(T^4 - T_{amb}^4)}{H_{abs}} - \frac{\varepsilon_{Sub} \cdot \sigma_{SB}(T^4 - T_{amb}^4)}{H_{abs}} \quad (8)$$

where τ_{Glass} is the glass transmittance, and ε_{Sub} is the equivalent thermal emittance relative to the absorber back-side and the vessel and it is assumed to be temperature independent. A previous work [43] has shown that for aluminum substrate $\varepsilon_{Sub} = 0.045$ provides an excellent fit to experimental data; it is in agreement with the thermal emittance calculated by FTIR measurement. Equation (8) was validated by using the MTB (the custom-made experimental setup described in Section 2.4), which allows us to evaluate the overall efficiency of the absorber by performing stagnation temperature measurements in high vacuum.

Figure 6a reports the Mirotherm[®] overall efficiency (as from Equation (8)) when placed in the MTB (blue solid line), the numerical simulation of the experimental setup (orange dash-dot line) and the overall efficiency experimentally measured using Equation (8) (black dots). The excellent agreement among numerical simulations, measured data obtained by Equation (6), and values descending from Equation (8) confirms that, if the conductive losses are negligible and the proper ε_{Sub} is taken in to account, the Equation (8) is a valid instrument to evaluate the overall absorber efficiency. Figure 6b shows the overall efficiency calculated from Equation (8) for the coating with different cut-off and an equivalent thermal emittance of aluminum substrate of 0.045. The equivalent substrate thermal emittance is assumed to be constant with temperature.

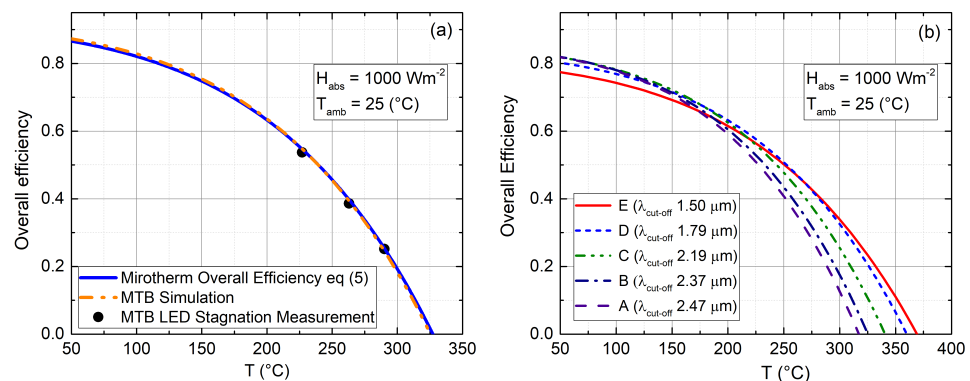


Figure 6. (a) Overall efficiency versus Absorber temperature T (°C): Mini-Test-Box (MTB) simulated efficiency (orange, dash dot), Led Measured MTB efficiency (black dots), Mirotherm[®] overall efficiency calculated using Equation (8) (blue solid line). (b) Overall efficiency calculated using Equation (8) for coating having cut-off as reported in Table 1 (see legend).

When estimating the overall efficiency for all the designed samples, it should be noted that the reduction in the $\lambda_{cut-off}$ affects in a less pronounced way the performances at low temperature, being all the values around 0.8 except for 1.5 μm case. In turn, when the temperature increases, the low thermal emittance plays a major role in preserving efficiency and, at temperature higher than 300 °C, the sample E shows the best performances with respect to the others and the stagnation temperature can be higher than 350 °C.

Moreover, it should be noted that for coating with $\lambda_{cut-off} < 2 \mu\text{m}$ the coating thermal emittance is lower than the industrial aluminum substrate emissivity. Hence the adoption of a substrate with a lower thermal emittance can significantly improve the efficiency. This result is not surprising: looking at the commercial absorber it is clear that the uncoated side of the absorber has a relative high roughness ($R_a = 1.65 \mu\text{m}$) and thermal emittance increases with roughness. The commercial absorbers have been developed for standard flat panels, for which the absorber uncoated side is insulated by rock wool, while the coated

side is in air or inert atmosphere and it is not useful to provide a better surface finishing to further reduce aluminum emissivity.

The multilayer E has been realized on aluminum on glass substrate and the experimental results are reported in Figure 7 as lines with square markers. In Figure 7a) are also reported the simulated spectral emissivity of the multilayer E (red line) and the experimentally measured spectral emissivity of aluminum on glass substrate (black line with diamond markers). Since the refractive indices of the materials used in the simulations were experimentally measured, an almost perfect agreement between the simulation and the measured emissivity is obtained.

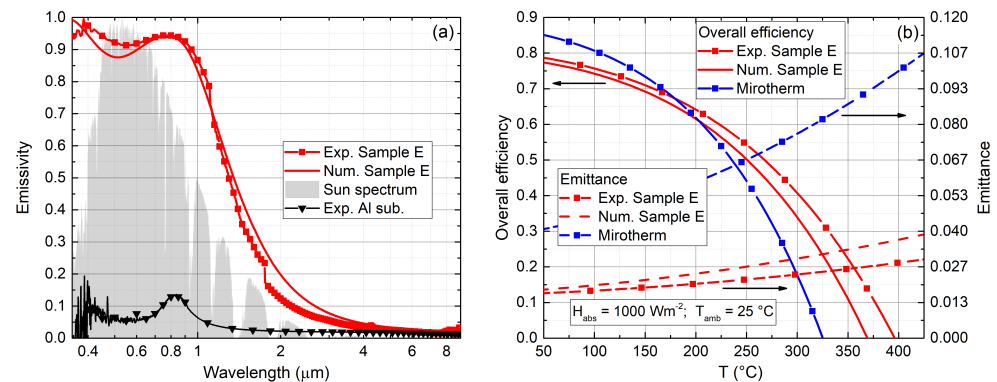


Figure 7. (a) The experimentally measured (red line with square markers) and numerically simulated (red line) spectral emissivity of the multilayer E. Black line with diamond markers is the experimentally measured spectral emissivity of the aluminum on glass substrate whereas the grey area represents the normalized Sun Spectrum. (b) Thermal emittance as function of temperature (right axis). On the left axis is reported the overall efficiency of the collector as function of absorber temperature according to Equation (8): $H_{abs} = 1000 \text{ Wm}^{-2}$, $\tau_{glass} = 0.91$ and $T_{amb} = 25 \text{ °C}$, with $\epsilon_{sub} = 0.045$ for the industrial aluminum substrate used in Mirotherm.

In Figure 7b) is reported on the right axis the temperature dependent thermal emittance $\epsilon(T)$ of the deposited multilayers (red dashed lines with square dots). The multilayer has a thermal emittance slightly lower than the numerical simulation (red dashed line).

On the left axis of Figure 7b) is also reported the overall efficiency calculated according to Equation (8) using the numerical simulation (red line) and experimental values of α and $\epsilon(T)$ (red line with square markers). The efficiency calculated from experimental values is higher than the calculated from numerical simulation, particularly at high temperatures, where the thermal emittance plays a major role. The improvement in efficiency and the stagnation temperature highlights the importance of thermal emittance and a well chosen cut-off. In particular, it is possible to achieve overall efficiency higher than 50% at temperature up to 267 °C and a stagnation temperature of 395 °C. In particular, at 260 °C the overall efficiency increases from 41% of Mirotherm to 52% with optimized coatings, resulting in 25% relative increase.

It is interesting to note that due to the entropy not all radiation is available for useful work [46] and this introduces the concept of exergy analysis which is of particular importance in the case of photovoltaic panels. However, the exergy analysis is beyond the scope of the present work.

Finally, it is worth remembering that our results have been obtained on an aluminum on glass substrate with the aim to address the optical properties neglecting the roughness. Before to move to industrial production, the results have to be repeated on industrial substrates and ageing studies have to be performed.

4. Conclusions

Our results show that a reduction in thermal emittance is essential to reach high operating and/or high stagnation temperatures in solar thermal unconcentrated applications.

An efficiency of 52% can be achieved up to 260 °C with a 27% relative increase respect to the commercial absorber on aluminum. The stagnation temperature can also be increased to about 400 °C without concentration.

Such performances, if confirmed on industrial substrates, will allow HVFP to contribute to the energy transition from fossil fuels to renewable energy for efficient heat production. It is worth mentioning that using the presented absorber on aluminum industrial substrate the radiation losses from coating would represent only 35% of the total radiation losses at 300 °C and contribution from the uncoated aluminum side accounts for the remaining 65%. The HVFP performances would benefit from a substrate thermal emittance reduction. Such reduction could be obtained with a better finishing of the back side of the aluminum substrate or using a substrate with a lower thermal emittance (such as copper or silver).

Author Contributions: D.D.M. wrote the original draft; A.C., C.D., D.D.L., D.D.M. performed the experiments and analysed the data, D.D.M. and C.D. numerical simulation and multilayer optimization; E.D.G., M.M. and R.R. supervised the work and revised the manuscript. All authors have read and agreed to the published version of the manuscript.

Funding: The Ph.D. grants of D.D.L. and A.C. are funded by the PON2014-2020 “Dottorati innovativi con caratterizzazione industriale” program (XXXIV ciclo and XXXV ciclo respectively). The Ph.D. grant of one of the authors (D.D.M.) is funded by the CNR-Confindustria “Dottorati di Ricerca Industriali” program XXXIV ciclo.

Institutional Review Board Statement: Not applicable.

Informed Consent Statement: Not applicable.

Data Availability Statement: Data is contained within the article.

Conflicts of Interest: The authors declare no conflict of interest.

References

1. Chapman, A.J.; McLellan, B.C.; Tezuka, T. Prioritizing mitigation efforts considering co-benefits, equity and energy justice: Fossil fuel to renewable energy transition pathways. *Appl. Energy* **2018**, *219*, 187–198. [CrossRef]
2. Shahsavari, A.; Akbari, M. Potential of solar energy in developing countries for reducing energy-related emissions. *Renew. Sustain. Energy Rev.* **2018**, *90*, 275–291. [CrossRef]
3. Meinshausen, M.; Meinshausen, N.; Hare, W.; Raper, S.C.B.; Frieler, K.; Knutti, R.; Frame, D.J.; Allen, M.R. Greenhouse-gas emission targets for limiting global warming to 2 °C. *Nature* **2009**, *458*, 1158–1162. [CrossRef]
4. Fleiter, T.; Elsland, R.; Rehfeldt, M.; Steinbach, J.; Reiter, U.; Catenazzi, G.; Jakob, M.; Rutten, C.; Harmsen, R.; Dittmann, F.; et al. Profile of heating and cooling demand in 2015. Heat Roadmap Europe. 2017. Available online: www.heatroadmap.eu (accessed on 5 February 2021).
5. Kranzl, L.; Hartner, M.; Müller, A.; Resch, G.; Fritz, S.; Fleiter, T.; Herbst, A.; Rehfeldt, M.; Manz, P.; Zubaryeva, A.; et al. Heating & Cooling Outlook until 2050, EU-28. 2018. Available online: https://www.hotmaps-project.eu/wp-content/uploads/2018/05/Hotmaps_D5-2_v16_2019-03-01.pdf (accessed on 5 February 2021).
6. Lauterbach, C.; Schmitt, B.; Jordan, U.; Vajen, K. The potential of solar heat for industrial processes in Germany. *Renew. Sustain. Energy Rev.* **2012**, *16*, 5121–5130. [CrossRef]
7. Weinstein, L.A.; Loomis, J.; Bhatia, B.; Bierman, D.M.; Wang, E.N.; Chen, G. Concentrating Solar Power. *Chem. Rev.* **2015**, *115*, 12797–12838. [CrossRef]
8. Kumagai, T.; To, N.; Balčytis, A.; Seniutinas, G.; Juodkasis, S.; Nishijima, Y. Kirchhoff’s Thermal Radiation from Lithography-Free Black Metals. *Micromachines* **2020**, *11*, 824. [CrossRef]
9. Nishijima, Y.; Balčytis, A.; Naganuma, S.; Seniutinas, G.; Juodkasis, S. Kirchhoff’s metasurfaces towards efficient photo-thermal energy conversion. *Sci. Rep.* **2019**, *9*, 8284. [CrossRef]
10. Wang, W.; Wen, H.; Huan, X.; Shi, J.; Li, Z.; Su, J.; Wang, C. Single layer WO_x films for efficient solar selective absorber. *Mater. Des.* **2020**, *186*, 108351. [CrossRef]
11. Bermel, P.; Lee, J.; Joannopoulos, J.D.; Celanovic, I.; Soljačić, M. Selective solar absorbers. *Annu. Rev. Heat Transf.* **2012**, *15*. [CrossRef]
12. Ning, Y.; Wang, J.; Ou, C.; Sun, C.; Hao, Z.; Xiong, B.; Wang, L.; Han, Y.; Li, H.; Luo, Y. NiCr–MgF₂ spectrally selective solar absorber with ultra-high solar absorptance and low thermal emittance. *Sol. Energy Mater. Sol. Cells* **2020**, *206*, 110219. [CrossRef]
13. Cao, F.; McEnaney, K.; Chen, G.; Ren, Z. A review of cermet-based spectrally selective solar absorbers. *Energy Environ. Sci.* **2014**, *7*, 1615–1627. [CrossRef]

14. Atchuta, S.R.; Sakthivel, S.; Barshilia, H.C. Selective properties of high-temperature stable spinel absorber coatings for concentrated solar thermal application. *Sol. Energy* **2020**, *199*, 453–459. [CrossRef]
15. Xu, K.; Du, M.; Hao, L.; Mi, J.; Yu, Q.; Li, S. A review of high-temperature selective absorbing coatings for solar thermal applications. *J. Mater.* **2020**, *6*, 167–182. [CrossRef]
16. Selvakumar, N.; Barshilia, H.C. Review of physical vapor deposited (PVD) spectrally selective coatings for mid- and high-temperature solar thermal applications. *Sol. Energy Mater. Sol. Cells* **2012**, *98*, 1–23. [CrossRef]
17. Yang, D.; Zhao, X.; Liu, Y.; Li, J.; Liu, H.; Hu, X.; Li, Z.; Zhang, J.; Guo, J.; Chen, Y.; et al. Enhanced thermal stability of solar selective absorber based on nano-multilayered AlCrSiO films. *Sol. Energy Mater. Sol. Cells* **2020**, *207*, 110331. [CrossRef]
18. Khelifa, A.B.; Khamlich, S.; Nuru, Z.Y.; Kotsedi, L.; Mebrahtu, A.; Balgouthi, M.; Guizani, A.A.; Dimassi, W.; Maaza, M. Growth and characterization of spectrally selective Cr₂O₃/Cr/Cr₂O₃ multilayered solar absorber by e-beam evaporation. *J. Alloys Compd.* **2018**, *734*, 204–209. [CrossRef]
19. Tsai, T.K.; Li, Y.H.; Fang, J.S. Spectral properties and thermal stability of CrN/CrON/Al₂O₃ spectrally selective coating. *Thin Solid Film.* **2016**, *615*, 91–96. [CrossRef]
20. Khoza, N.; Nuru, Z.Y.; Sackey, J.; Kotsedi, L.; Matinise, N.; Ndlangamandla, C.; Maaza, M. Structural and optical properties of ZrO_x/Zr/ZrO_x/Al_xO_y multilayered coatings as selective solar absorbers. *J. Alloys Compd.* **2019**, *773*, 975–979. [CrossRef]
21. Qiu, X.L.; Gao, X.H.; He, C.Y.; Liu, G. Optical design, thermal shock resistance and failure mechanism of a novel multilayer spectrally selective absorber coating based on HfB₂ and ZrB₂. *Sol. Energy Mater. Sol. Cells* **2020**, *211*, 110533. [CrossRef]
22. Lin, K.T.; Lin, H.; Yang, T.; Jia, B. Structured graphene metamaterial selective absorbers for high efficiency and omnidirectional solar thermal energy conversion. *Nat. Commun.* **2020**, *11*, 1–10. [CrossRef]
23. Yang, H.; Wang, Q.; Huang, Y.; Feng, J.; Ao, X.; Hu, M.; Pei, G. Spectral optimization of solar selective absorbing coating for parabolic trough receiver. *Energy* **2019**, *183*, 639–650. [CrossRef]
24. Thomas, N.H.; Chen, Z.; Fan, S.; Minnich, A.J. Semiconductor-based Multilayer Selective Solar Absorber for Unconcentrated Solar Thermal Energy Conversion. *Sci. Rep.* **2017**, *7*, 5362.10.1038/s41598-017-05235-x. [CrossRef]
25. Benz, N.; Beikircher, T. High efficiency evacuated flat plate solar collector for process steam production. *Sol. Energy* **1999**, *65*, 111–118. [CrossRef]
26. TVPSolar. Available online: <https://www.tvpsolar.com> (accessed on 5 February 2021).
27. Buonomano, A.; Calise, F.; d’Accadia, M.D.; Ferruzzi, G.; Frascogna, S.; Palombo, A.; Russo, R.; Scarpellino, M. Experimental analysis and dynamic simulation of a novel high-temperature solar cooling system. *Energy Convers. Manag.* **2016**, *109*, 19–39. [CrossRef]
28. Alanod. Available online: <https://alanod.com/en/products> (accessed on 5 February 2021).
29. Almeco Group. Available online: <https://www.almecogroup.com> (accessed on 5 February 2021).
30. Palmieri, V.G. Chief technical Officer TVPSolar. Personal communication.
31. Moss, R.; Henshall, P.; Arya, F.; Shire, G.; Eames, P.; Hyde, T. Simulator testing of evacuated flat plate solar collectors for industrial heat and building integration. *Sol. Energy* **2018**, *164*, 109–118. [CrossRef]
32. Moss, R.; Henshall, P.; Arya, F.; Shire, G.; Hyde, T.; Eames, P. Performance and operational effectiveness of evacuated flat plate solar collectors compared with conventional thermal, PVT and PV panels. *Appl. Energy* **2018**, *216*, 588–601. [CrossRef]
33. Li, X.F.; Chen, Y.R.; Miao, J.; Zhou, P.; Zheng, Y.X.; Chen, L.Y.; Lee, Y.P. High solar absorption of a multilayered thin film structure. *Opt. Express* **2007**, *15*, 1907–1912. [CrossRef]
34. Khelifa, A.B.; Soum-Glaude, A.; Khamlich, S.; Glénat, H.; Balghouthi, M.; Guizani, A.A.; Maaza, M.; Dimassi, W. Optical simulation, characterization and thermal stability of Cr₂O₃/Cr/Cr₂O₃ multilayer solar selective absorber coatings. *J. Alloys Compd.* **2019**, *783*, 533–544. [CrossRef]
35. Zhou, W.X.; Shen, Y.; Hu, E.T.; Zhao, Y.; Sheng, M.Y.; Zheng, Y.X.; Wang, S.Y.; Lee, Y.P.; Wang, C.Z.; Lynch, D.W.; et al. Nano-Cr-film-based solar selective absorber with high photo-thermal conversion efficiency and good thermal stability. *Opt. Express* **2012**, *20*, 28953–28962. [CrossRef] [PubMed]
36. D’Alessandro, C.; De Maio, D.; De Luca, D.; di Gennaro, E.; Giofrè, M.; Iodice, M.; Musto, M.; Rotondo, G.; Dalena, D.; Russo, R. Solar Selective Coating for Thermal Applications. *Key Eng. Mater.* **2019**. [CrossRef]
37. Forouhi, A.R.; Bloomer, I. Optical dispersion relations for amorphous semiconductors and amorphous dielectrics. *Phys. Rev. B* **1986**, *34*, 7018–7026. [CrossRef]
38. Rakić, A.D. Algorithm for the determination of intrinsic optical constants of metal films: application to aluminum. *Appl. Opt.* **1995**, *34*, 4755–4767. [CrossRef]
39. Boidin, R.; Halenkovič, T.; Nazabal, V.; Beneš, L.; Němec, P. Pulsed laser deposited alumina thin films. *Ceram. Int.* **2016**, *42*, 1177–1182. [CrossRef]
40. Gao, L.; Lemarchand, F.; Lequime, M. Exploitation of multiple incidences spectrometric measurements for thin film reverse engineering. *Opt. Express* **2012**, *20*, 15734–15751. [CrossRef]
41. Windt, D.L. IMD—Software for modeling the optical properties of multilayer films. *Comput. Phys.* **1998**, *12*, 360–370. [CrossRef]
42. Russo, R.; Monti, M.; Giamberardino, F.d.; Palmieri, V.G. Characterization of selective solar absorber under high vacuum. *Opt. Express* **2018**, *26*, A480–A486. [CrossRef] [PubMed]

43. Russo, R.; Monti, M.; D'Alessandro, C.; De Maio, D.; Musto, M.; Koral, C.; Andreone, A.; Di Giamberardino, F.; Palmieri, V. The Absorptance of Selective Solar Absorber Working in High Vacuum. In Proceedings of the 20th Italian National Conference on Photonic Technologies (Fotonica 2018), Lecce, Italy, 23–25 May 2018; Institution of Engineering and Technology: Lecce, Italy, 2018; pp. 56–64.10.1049/cp.2018.1665. [[CrossRef](#)]
44. De Maio, D.; D'Alessandro, C.; De Luca, D.; Musto, M.; Di Gennaro, E.; Rotondo, G.; Russo, R. Thermal Efficiency of a Concentrating Solar Collector Under High-Vacuum. *J. Phys. Conf. Ser.* **2020**, *1599*, 012029. [[CrossRef](#)]
45. D'Alessandro, C.; De Maio, D.; Mundo, T.; Musto, M.; Di Giamberardino, F.; Monti, M.; Dalena, D.; Palmieri, V.; De Luca, D.; Di Gennaro, E.; et al. Low Cost High Intensity LED Illumination Device for High Uniformity Laboratory Purposes. *Preprint* **2020**. [[CrossRef](#)]
46. Delgado-Bonal, A. Entropy of radiation: the unseen side of light. *Sci. Rep.* **2017**, *7*, 1642. [[CrossRef](#)]